nature communications

Article

https://doi.org/10.1038/s41467-025-58756-9

# A redox-active polymeric network facilitates electrified reactive-capture electrosynthesis to multi-carbon products from dilute $CO_2$-containing streams

Received: 29 April 2024

Accepted: 28 March 2025

Published online: 15 April 2025

Check for updates

Jinqiang Zhang[1,2,3,7], Yufei Cao[1,4,7], Pengfei Ou[1,7], Geonhui Lee[1,5,7], Yufei Zhao[1,3,7], Shijie Liu[2], Erfan Shirzadi[1], Roham Dorakhan[1], Ke Xie[1], Cong Tian[1], Yuanjun Chen[1], Xiaoyan Li[1], Yurou Celine Xiao[2], Ali Shayesteh Zeraati[2], Rui Kai Miao[2], Sungjin Park[1], Colin P. O'Brien[2], Jun Ge[4], Xin Zhou[6], David Sinton[2] ✉ & Edward H. Sargent[1] ✉

Reactive capture – the integration of $CO_2$ capture with electrochemical upgrade – offers the prospect of improving overall energy efficiency in captured-$CO_2$-to-fuels by eliminating the gas-phase $CO_2$ desorption step, and by further offering a $CO_2$-free gas product stream. Two related challenges limit the potential impact of electrified reactive capture today: its propensity to produce lower-value $C_1$ products (carbon products containing one carbon atom per molecule); and its failure to retain performance when fed dilute streams (e.g. ~1-10% $CO_2$). We posit that these could be addressed using catalysts that locally concentrate and activate in-situ generated $CO_2$: we integrate a redox-active polymeric network whose polymer fragments undergo reversible reduction during the electrochemical conversion process, enabling electron transfer to $CO_2$ molecules generated in-situ from carbonate capture liquid. We report as a result a 55 ± 5% $C_{2+}$ (carbon products containing two or more carbon atoms per molecule) Faradaic efficiency (FE) at 300 mA/cm$^2$ in an electrochemical reactive capture system in which the electrolysis stage is fed with 1 M $K_2CO_3$. We obtain 56 ± 4 wt% $C_2H_4$ in the product gas stream. When we use a dilute stream consisting of 1% $CO_2$ in $N_2$ at the KOH capture stage, we retain the $C_{2+}$ FE to within 85% (relative) of its value achieved in the case of pure $CO_2$.

It is of interest to utilize $CO_2$ captured from air, and to upgrade it into chemicals and fuels through thermochemical or electrochemical pathways[1–4]. Reactive capture offers the prospect of reducing the costs associated with $CO_2$ regeneration, purification, storage, and transport. It also has the potential to reduce separation costs, since it can be used to minimize $CO_2$ in the reactor outlet (Fig. S1)[5–8].

To date, reactive capture has yielded mostly $C_1$ products such as CO, formate, and methanol. Multi-carbon products such as ethylene, ethanol, and propanol are of interest[9–13]. An additional opportunity for improvement over prior reactive capture systems resides in their failure to retain performance when fed dilute e.g. ~1-10 % $CO_2$ streams due to the high pH of the generated capture liquid.

A full list of affiliations appears at the end of the paper. ✉e-mail: sinton@mie.utoronto.ca; ted.sargent@utoronto.ca

Here we focused on the design of catalysts that would prefer $C_{2+}$ production over hydrogen evolution reaction (HER) and $C_1$ products. Seeking a system that operated on dilute $CO_2$ streams, we posited that a catalyst that could trap $CO_2$ molecules to create a locally $CO_2$-rich environment could also serve to activate the in-situ generated $CO_2$.

A polymeric network consisting of redox-active viologen branches could be a suitable candidate for this role (Fig. 1a, b)[14,15]. By introducing non-conjugated $sp^3$ hybridized methylene groups (-$CH_2$-) connecting these viologen branches, we would seek to create a three-dimensional (3D) molecular network capable of trapping $CO_2$ and transporting electrons to the $CO_2$ molecules at reductive potentials[16,17].

We studied the new catalyst (PTV and Cu ensemble) in the context of an integrated reactive capture system that utilizes protons from a bipolar membrane (BPM) to convert carbonate (capture liquid) to $CO_2$ (Figs. S2–3)[7,18,19]. We synthesized a viologen-based polymer catalyst (PTV) via a one-step reaction from 1,3,5-tris(bromomethyl)benzene and 4,4′-dipyridyl in dimethylformamide (DMF) solution at 80 °C, yielding solid powders (Fig. S4)[20]. The viologen structures feature conjugated viologen branches connected to the benzene joints via non-conjugated -$CH_2$-, forming a stacked 3D polymeric network due to a steric hindrance effect between the branches (Fig. S5).

## Results and discussion

### Local enrichment and capture of $CO_2$

Molecular dynamics (MD) simulations show that $CO_2$ is prone to diffuse into the polymeric structure of PTV and become trapped, thus suppressing its migration outside the network (Fig. 1d, Supplementary Data 1 and 2). Compared to the distribution of $CO_2$ molecules on a bare Cu surface (Fig. 1c, Supplementary Data 1 and 3), the PTV-loaded electrode displays a higher $CO_2$ concentration close to the surface of the electrode (Fig. 1e), suggesting the potential to steer reactions in a $CO_2$-lean environment (Fig. S6). We were encouraged that the high local $CO_2$ concentration in the inner Helmholtz plane (IHP) may suppress the competing HER and thus promote $C_{2+}$ production[21,22].

### Redox behaviour to activate $CO_2$

The redox properties of the viologen species, studied using cyclic voltammetry, also suggested its potential to bridge electron transfer to $CO_2$. As shown in Fig. 1f, the PTV electrode displays two pairs of redox peaks centered at 0.4 V and 0 V *vs.* RHE, the first and second reduction/oxidation of the viologen moieties. The redox reactions are highly reversible and can operate at high current densities over multiple cycles (Figs. S7–8). When $CO_2$ is introduced to the system, the reduction peaks of PTV increase accordingly, while the oxidation peaks remain unchanged. This suggests that the reduced forms of viologen species in PTV are capable of transferring electrons to $CO_2$ molecules to initiate the activating process, forming $CO_2$-adduct thereon. The reduction peaks related to $CO_2$ activation on the PTV catalyst are shifted to a higher potential, consistent with the lower activation energy required. The first electron reduction of $CO_2$ molecules is usually the most energy-consuming step for CO2RR, so this approach has the potential to support the reduction of $CO_2$ to $C_{2+}$ products[23].

Using density functional theory (DFT), we calculated the stepwise reduction potential of $CO_2$ with and without the PTV catalyst. We used the viologen fragments (PV) in the polymer structure within the simulation since these are posited to be the active species in PTV. To ensure that this model aligns with experimental conditions, we have also considered additional factors, including the polymeric nature of PTV, the Cu-polymer interface, the role of $K^+$ in the electrolyte, and the reduction of PTV on the electrode during the modelling. Both the one-electron and two-electron reduction of PTV occur (Table S1) before the one-electron reduction of $CO_2$, enabling viologen to accept electrons and then transfer them to $CO_2$ (Fig. S9) with relatively low transition state barriers (TS1 and TS2). The reduction potentials of $CO_2$ show an improvement of 0.5 V with *vs.* without the PTV catalyst, *i.e.*, the 1 $e^-$ reduction of $CO_2$ is facilitated by PTV. This suggests the mechanism of Fig. 1g, where first the reduction of the viologen branches occurs, which then reacts with $CO_2$ molecules to form a PTV-$CO_2$ complex (Fig. S10), with a free energy of 0.78 eV[17,24,25]. A subsequent single-electron reduction of the complex takes place at −1.5 V *vs.* RHE (compared to -2.0 V of $CO_2$ one-electron reduction potential, Table S1). The dissociation of the reduced complex produces $CO_2^-$ – the first single-electron reduction product of $CO_2$ at a lower reductive potential. The released viologen branches are free to interact with $CO_2$ molecules in the subsequent cycles. The process reduces $CO_2$ to form $CO_2^-$ at a lower potential, and supports their further reduction to $C_{2+}$ products when the intermediates are transferred to the Cu.

We carried out in-situ Raman spectroscopy in a $CO_2$ cell: here we found that the PTV-Cu electrode shows additional peaks in the range of 1250–1750 $cm^{-1}$. These we assign to vibrational fingerprints of $CO_2^-$ (Figs. 2a, b and S11). The peaks appear in the initial scan and remain visible even when scanned to the negative potentials, consistent with an activating role for PTV[26,27]. The major bands related to surface-adsorbed *CO at 300 - 500 and 1900 - 2100 $cm^{-1}$ appear earlier at the relatively more positive potential on the PTV-Cu electrode, compared to those on Cu (0.17 V *vs.* -0.23 V RHE) (Fig. 2a, b)[26]. This agrees with a picture in which the activation of $CO_2$ facilitates the conversion to $C_{2+}$ products at lower potentials when in the presence of PTV. A similar trend is found with in-situ Fourier transform infrared spectroscopy (FTIR), where peaks associated with the activated $CO_2$ species around 1643 $cm^{-1}$ ($CO_2^-$ and *COOH) appear earlier on PTV-Cu than on bare Cu (Figs. 2c, d and S12)[28,29].

### Performance in electrified reactive capture

We carried out linear sweep voltammetry (LSV, Figs. 3a and S13) with in-situ differential electrochemical mass spectrometry (DEMS) in the presence of a $CO_2$ atmosphere. The PTV catalyst (PTV-Cu) exhibits a lower onset potential compared to the bare Cu electrode (Fig. 3a). Although similar current densities were achieved on both electrodes, HER was dominant on the bare Cu electrode. On bare Cu, $H_2$ evolution occurs at the onset potential; and a higher driving force is required for $C_2H_4$ evolution. On the PTV-Cu electrode, $H_2$ evolution is suppressed and $C_2H_4$ evolution appears earlier, suggesting an improved capability to convert $CO_2$ and reduce HER kinetics (Figs. S13–14).

We then studied reactive capture in a system in which $CO_2$ is captured by KOH to form $K_2CO_3$. We adopted an interposer design using mixed cellulose esters (MCE) to create a pH gradient, where the cation exchange layer/interposer interface is acidic for the reaction between carbonate ions and protons to generate $CO_2$; while the pH on the electrode is alkaline (pH > 13) for the conversion of $CO_2$ to $C_{2+}$ (Figs. S3 and S15)[30]. The continuous microporous structure allows the transport of $CO_2$ from the layer to the surface of the electrode to support conversion reactions.

In a carbonate reduction system with $K_2CO_3$ simulating the post-capture liquid, the PTV-Cu showed an increase in FE to $C_{2+}$ products compared to bare Cu, especially on 300 mA $cm^{-2}$, where PTV-Cu shows FE of 47 ± 3% and bare Cu of 37 ± 3% (Fig. 3b and S16–19). PTV-Cu shows a decrease in hydrogen evolution, consistent with the capability of PTV to provide local enrichment of $CO_2$ and to activate $CO_2$ molecules, thus facilitating conversion to $C_{2+}$ products and a reduction in the local $H_2O$ presence and activity relevant to HER. Correspondingly, for a given potential of −5.0 V, the PTV-Cu showed a higher $J_{partial}$ of 135 ± 7 mA $cm^{-2}$ than the bare Cu electrode at $J_{partial}$ of 115 ± 5 mA $cm^{-2}$ at -5.5 V (Fig. 3c).

We then introduced carbon additives to address the low conductivity of PTV. We found carbon black (CB) nanoparticles to be more effective than carbon nanotubes (CNT) and reduced graphene oxide (rGO) (Fig. S20). We also incorporated a hydrophobic poly(cyclohexyl methacrylate) (PCHMA) polymeric layer to reduce the water content on the surface of the electrode (PCHMA-PTV/CB-Cu electrode), this optimization leading to a peak $FE_{C2+}$ over 50 % (Figs. 3d and S21–22).

https://doi.org/10.1038/s41467-025-58756-9

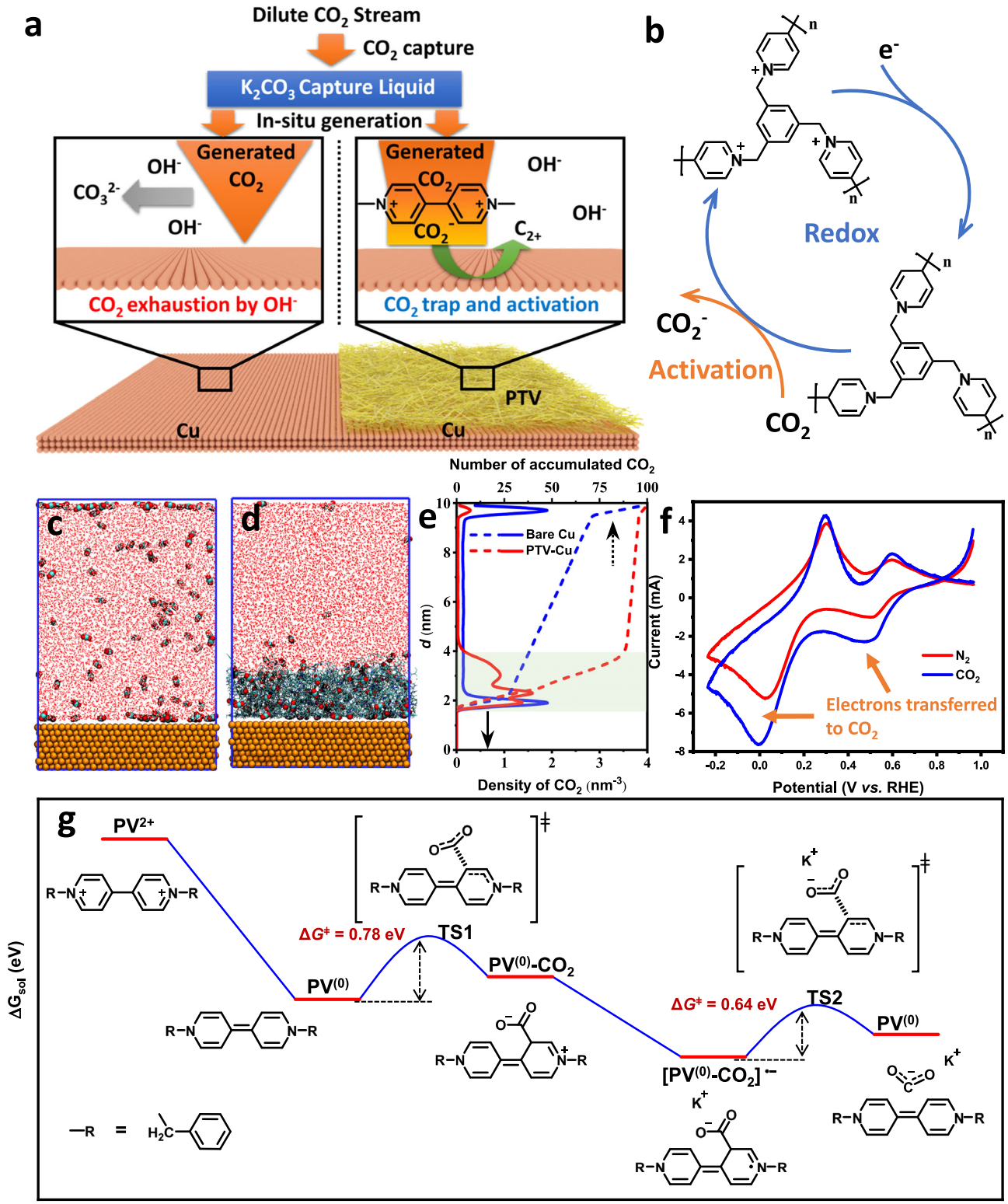


**Fig. 1 | The design of redox-active polymeric catalyst for $CO_2$ reactive capture by increasing local $CO_2$ concentration and achieving $CO_2$ activation.** The Schematic illustration of **a** polymeric viologen catalyst facilitating the conversion to $C_{2+}$ products via trapping and activating $CO_2$, and **b** the redox capability of PTV molecular structure with viologen branches to activate $CO_2$. **c**–**d**. The snapshots of the MD simulations of the $CO_2$ diffusion patterns in water on **c** bare Cu electrode and **d** PTV-Cu electrode. **e** Distribution of $CO_2$ molecules at the endpoint of the MD simulation in **c** and **d**. **f** CV curves of PTV-carbon electrode at $N_2$ and $CO_2$ atmosphere, respectively. The electrolyte is 1 M $K_2CO_3$. The scan rate is 100 mV $s^{-1}$. The potential is not iR corrected. **g** DFT calculations of $CO_2$ activation to $CO_2^{\cdot-}$ in the presence of PTV branches. TS is the transition state during the reaction.

https://doi.org/10.1038/s41467-025-58756-9

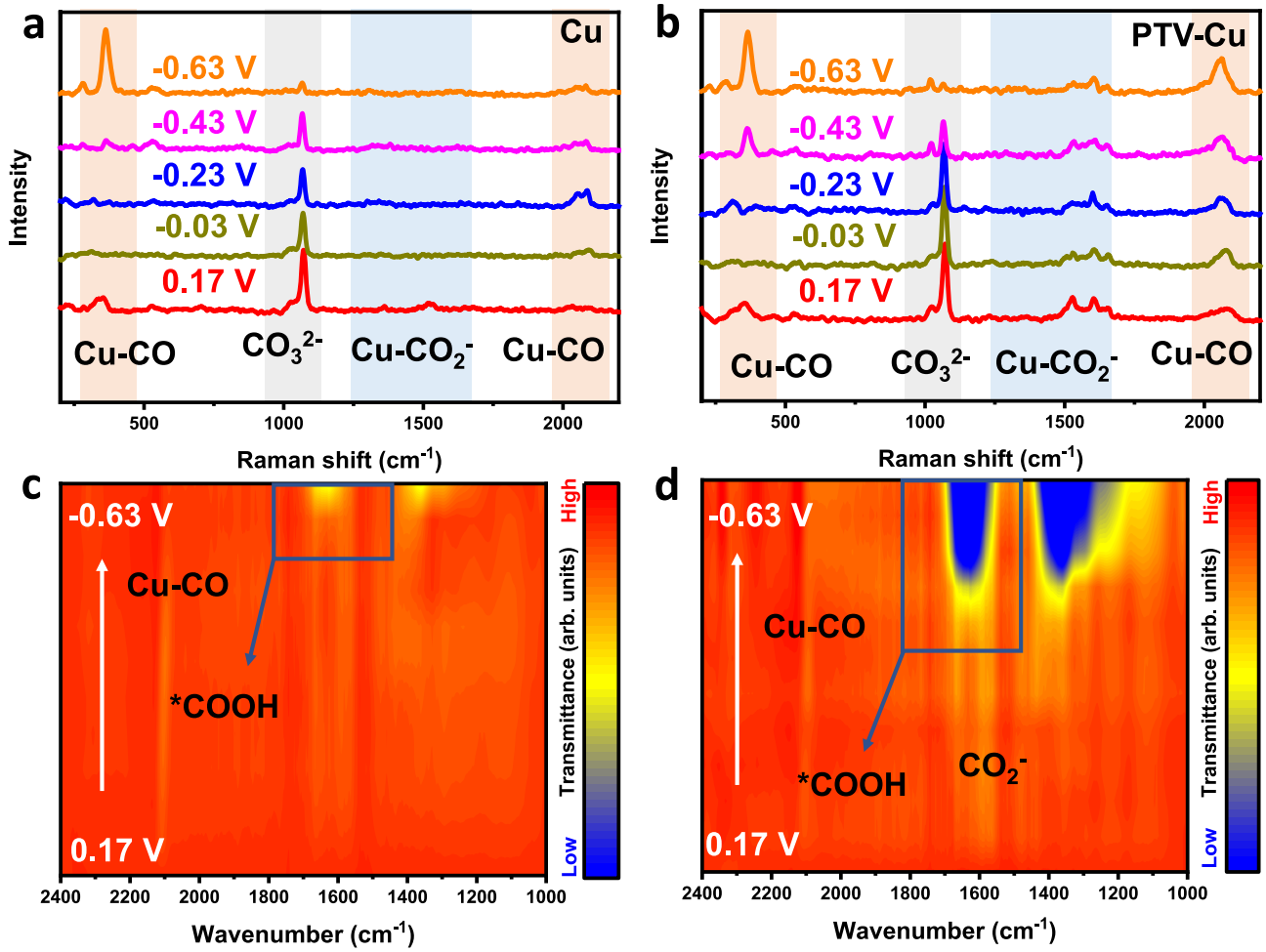


**Fig. 2 | Intermediate detection on the PTV-Cu electrode for $CO_2$ activation. a**, **b**. In-situ Raman spectra of **a**. bare Cu electrode and **b** PTV-Cu electrode scanning from 0.17 V to -0.63 V *vs*. RHE. **c**, **d**. In-situ FTIR spectra of **c** bare Cu electrode and **d** PTV-Cu electrode scanning from 0.17 to -0.63 V *vs*. RHE. The electrolytes used are 1 M $K_2CO_3$.

When we further optimized the anolyte and membrane, we reached $FE_{C2+}$ of 55 ± 5 % with a lower full cell voltage of -4.1 V (Fig. 3c, d and S23–25). The outlet had a $C_2H_4$ concentration of 56 ± 4 wt%.

### Performance in electrified reactive capture with diluted $CO_2$ stream

We captured $CO_2$ streams (concentrated 100% and diluted 1%) in 1 M KOH for 2 h. Employing capture liquid purged with pure $CO_2$ resulted in similar performance to the case of 1 M $K_2CO_3$ (Figs. 4a and S26). However, when 1% $CO_2$ was used, Cu showed a sharp decrease in $FE_{C2+}$, an effect we attribute to the lower conversion of KOH into $K_2CO_3$ (Fig. S27). PTV-Cu maintained a $C_{2+}$ FE of 45 ± 5 %, by contrast, owing to a high local $CO_2$ concentration and conversion rate from the capability of trapping and activating $CO_2$. We demonstrated this by further perturbing the capture solution pH, mixing KOH into $K_2CO_3$ (Movie S1), and found PTV-Cu to have a greater tolerance for high pH capture solution (Figs. 4b and S28).

In the stability test of carbonate reduction at 300 mA $cm^{-2}$ (Fig. S29), we found that the MCE buffer layer was damaged by high pH on the electrode (Figs. S30–34). We replaced the MCE buffer layer with polydopamine-coated poly(methyl methacrylate) (PDA-PMMA) microspheres as the interposer (Figs. S35–38). The stacking of PMMA spheres generated pores suitable for $CO_2$ transportation and catholyte flow while the Nafion coating provided a more uniform distribution of protons (Fig. 4c)[31]. We constructed a reactive capture system in which $CO_2$ is continuously captured by $OH^-$, thus balancing pH and forming carbonate to feed the electrolysis process (Fig. 4d). An integrated capture-conversion system operates continuously for 40 h at a current density of 300 mA $cm^{-2}$, with stable full cell voltage and $C_{2+}$ FE ~ 50 % (Figs. 4e and S39–40).

In summary, a polymeric network of redox-active branches is designed to facilitate $CO_2$ reactive capture. The polymeric catalyst can increase local $CO_2$ concentration and activate $CO_2$ during the reduction process. As a result, the electrochemical performance of $CO_2$ reactive capture from KOH can be significantly enhanced, especially in a $CO_2$-lean capture environment. The system is able to produce a peak $C_{2+}$ FE of 55 ± 5 % at 300 mA $cm^{-2}$ with a 56 ± 4 wt% $C_2H_4$ in the outlet stream. This system is capable of continuously capturing $CO_2$ to be converted to $C_{2+}$ products over 40 h.

## Methods

### Material synthesis

**Synthesis of PTV.** The synthesis of PTV was conducted based on the previously published ref. 20. Typically, 1,3,5-tris(bromomethyl)benzene (1 mmol, Sigma-Aldrich, 97%), 4,4′-bipyridine (1.5 mmol, Sigma-Aldrich), and polyethylene-block-poly(ethylene glycol) (1.0 g, Sigma-Aldrich, $M_n$ ~ 1,400) were dissolved in 20 mL N, N-dimethylformamide (DMF, Sigma-Aldrich, 99.8%). The solution was kept stirring at 80 °C for 3 h. The precipitates were filtered and washed with DMF, methanol (Sigma-Aldrich, 99.8%), and water. The product was dried under vacuum to give yellowish-brown powders.

**Synthesis of PCHMA.** The synthesis of PCHMA was achieved by a polymerization technique on cyclohexyl methacrylate. Typically,

https://doi.org/10.1038/s41467-025-58756-9

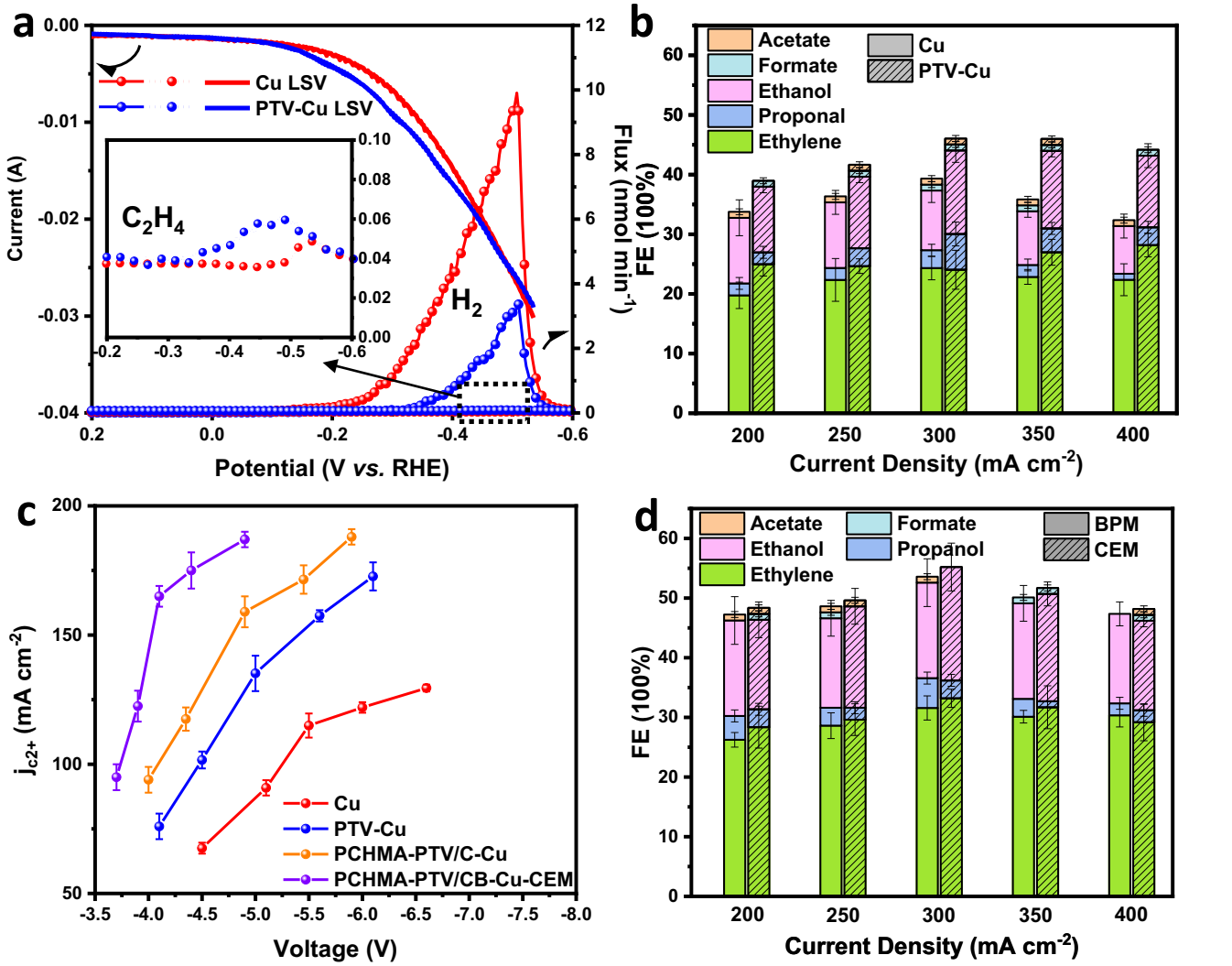


**Fig. 3 | Electrochemical performance of reactive capture to $C_{2+}$ products with PTV catalyst. a** The LSV curves of bare Cu and PTV-Cu electrodes at a scan rate of 100 mV s$^{-1}$, and the corresponding in-situ DEMS results of $H_2$ evolution. The inset image is the in-situ DEMS results of $C_2H_4$ evolution at the same condition. The potential is not iR corrected. **b** Product distribution for the electrochemical conversion of 1 M $K_2CO_3$ solution at current densities from 200 to 400 mA cm$^{-2}$ using bare Cu and PTV-Cu electrodes. **c** The corresponding full cell j-V curve from the performance in **b** and **d**. The potential is not iR corrected. **d** Product distribution for the electrochemical conversion of 1 M $K_2CO_3$ solution at current densities from 200 to 400 mA cm$^{-2}$ with PCHMA-PTV/CB-Cu electrode with alkaline anolyte with BPM and acidic anolyte with CEM, respectively.

cyclohexyl methacrylate (10 mmol, Sigma-Aldrich, 97%) and 2,2′-azobisisobutyronitrile (AIBN, 0.2 g, Sigma-Aldrich, 12 wt.%) were dissolved in 6 mL acetic acid (Sigma-Aldrich, 99.7%) at 70 °C overnight under $N_2$ atmosphere. The mixture was then added to 50 mL diethyl ether (Sigma-Aldrich, 99.0%) to generate precipitation. The white product PCHMA was achieved by washing with diethyl ether and drying under vacuum.

**Synthesis of PDA-PMMA microsphere**. The synthesis of PDA-PMMA contains two major steps: the preparation of PMMA microspheres and the coating of the PMMA microspheres with PDA. The PMMA microspheres are prepared based on the previously published ref. 32,33. Typically, a solution of 15 mL methyl methacrylate (MMA, Sigma-Aldrich, 99%), 12 mg sodium dodecyl sulfate (SDS, Sigma-Aldrich, 99.0%) as the surfactant, and 116.9 mg potassium persulfate (Sigma-Aldrich, 99.0%) as the initiator in 175 mL water was prepared and kept at 70 °C under $N_2$ and stirring for 4 h. After the solution turned milky white colloidal solution, it was dried under ambient conditions.

The coating of PDA to PMMA microspheres was performed by dispersing 150 mg PMMA microspheres and 46 mg dopamine (Sigma-Aldrich) in a Tris buffer (pH = 10, Sigma-Aldrich). A solution of ammonium persulfate (68.4 mg, Sigma-Aldrich, 98.0%) was added dropwise to the dispersion. The polymerization was performed at stirring for 24 h. The resulting precipitates were washed with water and dried under vacuum. The interlayers were prepared by spraying a mixture of PDA-PMMA microspheres and Nafion dispersion (1 mg/10 µL, Sigma-Aldrich, 5 wt.%) in methanol to the surface of the electrodes.

### Electrode preparation

Cu catalysts (US Research Nanomaterials, Inc.) were prepared by spray-coating Cu nanoparticle ink onto carbon paper (Freudenberg H23, Fuel Cell Store). Cu nanoparticles (80 mg) were dispersed in a mixture of 12 mL methanol and 160 µL Nafion solution and then sonicated for 3 hours. The Cu nanoparticle ink was spray-coated on the carbon paper with a loading of ~4 mg/cm$^2$ and dried under atmospheric conditions. The Cu catalysts were used for electrochemical characterization

https://doi.org/10.1038/s41467-025-58756-9

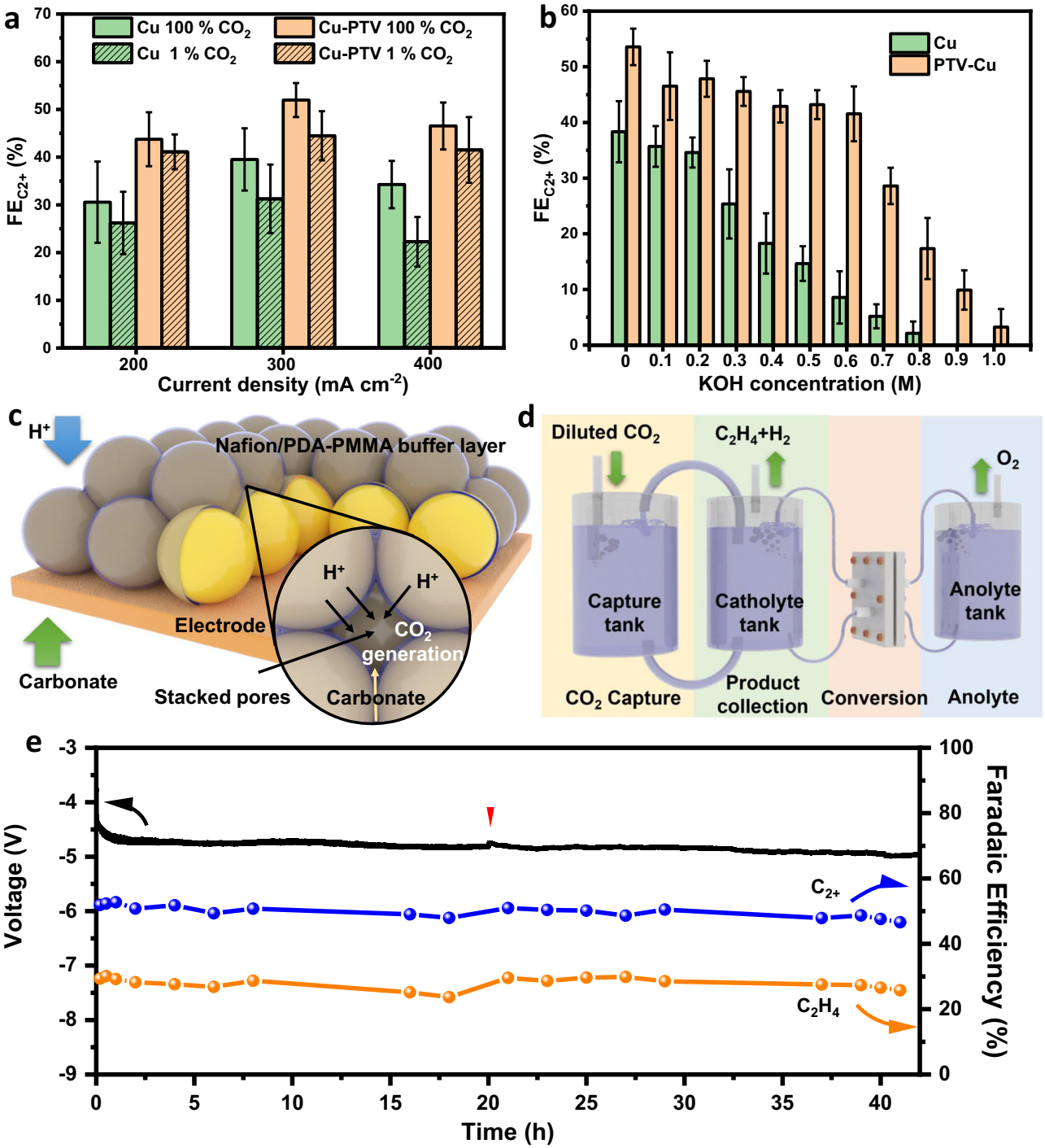


**Fig. 4 | Electrochemical performance of reactive capture using diluted $CO_2$ stream with PTV catalysts. a** The $C_{2+}$ product FE for the electrochemical conversion of the captured liquids at current densities from 200 to 400 mA $cm^{-2}$ using bare Cu and PTV-Cu electrodes. The captured liquids were prepared by purging different $CO_2$ streams (100 % and 1 %) in 1 M KOH for 2 h. **b** The $C_{2+}$ product FE for the electrochemical conversion of mixture liquids at the current densities of 300 mA $cm^{-2}$ using bare Cu and PTV-Cu electrodes. The mixtures were prepared by adding different concentrations of KOH in 1 M $K_2CO_3$ electrolyte. **c** Schematic illustration of the designed Nafion/PDA-PMMA buffer layer on the electrode promoting in-situ $CO_2$ generation. **d** The schematic illustration of an integrated system continuously capturing and converting $CO_2$ from diluted stream (1 %) to $C_{2+}$ products. **e** The Faradaic efficiencies of $C_{2+}$/$C_2H_4$, and full cell voltage for the long-term operation of the integrated system with the designed catalyst and buffer layer. The red arrow indicates the replacement of catholyte during the stability test. The electrolyte used is 1 M $K_2CO_3$. The potential is not iR corrected.

for carbonate electrolysis in a membrane electrode assembly (MEA) cell.

The fabrication of PTV-Cu electrodes was the same as that of Cu electrodes, with the additional layer of PTV sprayed on the surface of Cu electrodes. The PTV dispersion was prepared by mixing PTV and Nafion (1 mg/5 μL) in methanol. PTV/carbon-Cu electrodes were prepared by mixing different types of carbon (CB, CNT or rGO) with PTV (1 mg/5 mg) through the same procedure. PCHMA-PTV/CB-Cu electrodes were prepared by spraying an additional layer of PCHMA on the surface of the PTV/CB-Cu electrodes. The PCHMA dispersion was prepared by mixing PCHMA and Nafion (1 mg/5 μL) in methanol.

### Characterizations

The morphologies of the materials and electrodes were conducted by field emission scanning electron microscopy (Hitachi, SU5000). Infrared spectroscopies were conducted on a Nicolet Magna 6700 FTIR spectrometer. All spectra were obtained using 4 $cm^{-1}$ resolution and 64 scans at room temperature.

In-situ Raman measurements were performed using a Renishaw inVia Raman Microscope (water immersion objective (×63), 785 nm laser) in a modified flow cell with 1 M $K_2CO_3$ aqueous solution as the electrolyte (pH 11.6 ± 0.1). The cell structure is shown in Fig. 41. The prepared catalytic cathode was used as the working electrode, Ag/AgCl reference electrode (freshly prepared 3 M KCl) was used as the reference electrode, and a platinum coil was used as the counter electrode. $CO_2$ was used as the reactant gas which was continuously supplied to the gas chamber during the measurement.

In-situ FTIR measurement was performed on Thermo Nicolet 6700 FTIR with MCT detector in a modified flow cell with 1 M $K_2CO_3$ aqueous solution as the electrolyte (pH 11.6 ± 0.1). The cell structure is shown in Fig. 41. The prepared cathode by dropping catalysts dispersion on Au substrate was used as the working electrode, Ag/AgCl reference electrode (freshly prepared 3 M KCl) was used as the reference electrode, and a carbon rod was used as the counter electrode. $CO_2$ was used as the reactant gas which was continuously supplied to the gas chamber during the measurement.

In-situ DEMS measurement was performed on a commercial magnetic sector mass spectrometer (Thermo Fischer) with a specially designed gas-purging system ($CO_2$ as carrier gas) in a modified flow cell with 1 M $K_2CO_3$ aqueous solution as the electrolyte. The cell structure is shown in Fig. 41. PTFE membrane (LingLu) with a porosity over 50% and pore diameters less than 20 nm have been used as the hydrophobic membrane. Pt wire was used as the counter electrode and Ag/AgCl (3 M KCl) was used as the reference electrode. The electrolyte was 1 M $K_2CO_3$ solution. The flow rate of purge gas was set at 1 mL $min^{-1}$. The ion current was set at 2000 mA with no corrections.

### Electrochemical tests

All the electrochemical tests are performed at room temperature (20-25 °C). The cyclic voltammetry (CV) tests were carried out using a flow cell configuration. Nickel foam served as the counter electrode, PTV electrode as the working electrode, 1 M $K_2CO_3$ as the electrolyte (pH 11.6 ± 0.1), an Ag/AgCl electrode (freshly prepared 3 M KCl) as the reference, and an anion exchange membrane as the separator. The measured potentials *vs.* Ag/AgCl were converted to the reversible hydrogen electrode (RHE) scale according to the Nernst equation:

$$E_{RHE} = E_{Ag/AgCl} + 0.059\,pH + E^{O}_{Ag/AgCl} \quad (1)$$

where $E_{RHE}$ is the converted potential *vs.* RHE, $E^{o}_{Ag/AgCl} = 0.197$ at 25 °C, and $E_{Ag/AgCl}$ is the experimentally measured potential against Ag/AgCl reference.

During CV tests, the flow of electrolytes was stopped to eliminate vortices, ensuring smooth CV curves. Tests were performed under both $N_2$ and $CO_2$ atmospheres, with varying scan rates. Electrochemical performance was evaluated using an electrochemical station (Autolab PGSTAT204, Metrohm) in an MEA system and a flow cell system. The All experiments were repeated three times to report the average and standard error. The electrolysis was held for at least 30 min to collect gas and liquid products. For the MEA system with carbonate electrolysis, the as-prepared electrode was used as the cathode with mixed cellulose ester (MCE) membrane as the buffer layer between the cathode and membrane. The anolyte was a 0.5 M $H_2SO_4$ solution (pH 0.3 ± 0.05). Nickel foam was used as the anode for oxygen evolution reaction (OER) in the BPM system. Titanium foam-supported iridium oxide ($IrO_x$/Ti) was used as the anode catalyst for OER in the CEM system. Bipolar membrane was used to separate two electrodes in the BPM system. Nafion 117 membrane was used to separate the two electrodes in the CEM system. These membranes are purchased from fuel cell stores. Nafion 117 membranes are treated with sulfuric acid and BPM are treated with 1 M KCl solution overnight. The catholyte and anolyte were circulated using a peristaltic pump. All the electrolytes are freshly prepared before use. The volume of the electrolytes is 50 mL for most tests, and 1 L for the stability tests. We used mass flow controllers (MFC) purchased from Sierra Instruments to measure all the gas flow.

The gas-phase products were analyzed using gas chromatography (GC) (Shimadzu 2014, PerkinElmer Clarus 580) equipped with a thermal conductivity detector (TCD) and a flame ionization detector (FID). The FEs for gaseous products were calculated as follows:

$$FE(\%) = \frac{NF \times (\nu/60) \times \left(y/24.5 \times 10^{9}\right)}{i} \times 100\% \quad (2)$$

Where $N$ represents the number of electrons required for products, y (ppm) represents the volume concentration of the gaseous product, $v$ (sccm) represents the measured gas flow rate, $i$ (A) represents the collected cell current, $F$ is the Faraday constant (96485 C $mol^{-1}$).

The liquid phase products were analyzed with a 600 MHz Agilent DD2 $^1$H NMR. All the gas and liquid measurements were repeated independently at least 3 times to report the average and standard error.

The detection limit of GC for gas-phase products is measured by varying the concentration of gas in the $CO_2$ stream. ppm level of the gas-phase product is injected three times. The area of a peak is linearly correlated to the concentration when the area value is plotted at the y-axis, and the concentration is at the x-axis. The intercept of the x-axis represents of detection limits of gas concentration. The detection limit of $CO_2$ is measured by injecting a different air volume from 1 mL to 5 mL. The $CO_2$ concentration in the air is assumed at 400 ppm. Two different $CO_2$ streams have been used for capturing: pure $CO_2$ stream (100 % $CO_2$) and 1% $CO_2$ mixed with 99% $N_2$ (1 % $CO_2$), which are realized by using two MFCs to control the flow rate of $CO_2$ and $N_2$. The total flow rate of the mixture gas was kept at 20 sccm. The 1 M KOH capture solution volume was 50 mL. The mixture gas was kept flowing into the capture solution for 2 h before being applied for electrochemical performance evaluation. We used the same cell setup as the carbonate reduction in an MEA system with a 1 $cm^2$ electrode.

### Calculations

**MD simulation.** All MD simulations were conducted using the GROMACS 2019.3[34]. Parameters for $CO_2$ and PTV were generated with the antechamber module of Amber18 using the general Amber force field (GAFF), with partial charges set to fit the electrostatic potential generated with B3LYP/6-31 G(d) by RESP[35,36]. The 12-6 LJ potential parameters of Cu were obtained from previous work. Heinz, et al. presented 12-6 and 9-6 Lennard-Jones (LJ) parameters for several face-centered cubic metals (Ag, Al, Au, Cu, Ni, Pb, Pd, Pt)[37]. The performance is comparable to tight-binding and embedded atom models and it has compatibility with widely used force fields. The electrode surface consists of 8 layers of 30 × 26 Cu (111) surface with 6240 atoms. The $CO_2$ molecules were initially placed at the top of the box and they gradually diffused to Cu upper surface. It simulated the process of $CO_2$ generated from the electrolyte and captured by the electrode. The system was placed in a periodic cubic box of water molecules represented by the three-point charge TIP3P model. The total system was energy minimized by a succession of steepest descent and conjugate gradient methods. Thereafter, it was equilibrated for 100 ns at constant temperature (298.15 K) and pressure (1 bar) (NPT). We used V-rescale thermostat and Parrinello–Rahman barostat to keep the temperature and pressure constant, respectively[38,39]. The cutoff radius for neighbor searching and nonbonded interactions was taken to be

12 Å, and all bonds were constrained using the LINCS algorithm. All computed structures in MD simulations were illustrated using VMD[40,41].

**DFT calculations**. All the calculations were carried out with the Gaussian 16 package. Geometry optimizations were performed with M06-2X exchange-correlation functional[42]. The 6-31 G(d) basis set was used for all atoms[43]. Frequency analysis was conducted at the same level of theory to verify the stationary points to be minima or saddle points. The single-point energies were computed with M06-2X /def2tzvp basis sets. To estimate the bulk solvent effects on the reaction, all the structures were optimized in the water solvent with the polarized continuum model using the integral equation formalism variant (IEFPCM)[44]. The relative energies with ZPE corrections and free energies (at 298.15 K and 1 atm pressure) are in eV. All Computed structures are illustrated using CYLView. We used the active viologen fragments in the polymeric structure as the simulation model to simplify the computational workload[45]. We have considered the polymeric nature of PTV, the Cu-polymer interface, the role of $K^+$ in the electrolyte, and the reduction of PTV on the electrode to ensure that this model aligns with experimental conditions.

## Data availability

All data are available in the main text or the supplementary materials. Source data are provided with this paper.

## References


1. Ozkan, M., Nayak, S. P., Ruiz, A. D. & Jiang, W. Current status and pillars of direct air capture technologies. *iScience* **25**, 103990 (2022).
2. Erans, M. et al. Direct air capture: process technology, techno-economic and socio-political challenges. *Energy Environ. Sci.* **15**, 1360–1405 (2022).
3. Sharifian, R., Wagterveld, R. M., Digdaya, I. A., Xiang, C. & Vermaas, D. A. Electrochemical carbon dioxide capture to close the carbon cycle. *Energy Environ. Sci.* **14**, 781–814 (2021).
4. Siegel, R. E., Pattanayak, S. & Berben, L. A. Reactive capture of $CO_2$: opportunities and challenges. *ACS Catal.* **13**, 766–784 (2023).
5. Sullivan, I. et al. Coupling electrochemical $CO_2$ conversion with $CO_2$ capture. *Nat. Catal.* **4**, 952–958 (2021).
6. Gutiérrez-Sánchez, O. et al. A state-of-the-art update on integrated $CO_2$ capture and electrochemical conversion systems. *ChemElectroChem* **9**, e202101540 (2022).
7. Xiao, Y. C. et al. Direct carbonate electrolysis into pure syngas. *EES Catal.* **1**, 54–61 (2023).
8. Li, M., Irtem, E., Iglesias van Montfort, H.-P., Abdinejad, M. & Burdyny, T. Energy comparison of sequential and integrated $CO_2$ capture and electrochemical conversion. *Nat. Commun.* **13**, 5398 (2022).
9. Muroyama, A. P. & Gubler, L. Carbonate regeneration using a membrane electrochemical cell for efficient $CO_2$ Capture. *ACS Sustain. Chem. Eng.* **10**, 16113–16117 (2022).
10. Dinh, C.-T., Li, Y. C. & Sargent, E. H. Boosting the single-pass conversion for renewable chemical electrosynthesis. *Joule* **3**, 13–15 (2019).
11. Weng, L.-C., Bell, A. T. & Weber, A. Z. Towards membrane-electrode assembly systems for $CO_2$ reduction: a modeling study. *Energy Environ. Sci.* **12**, 1950–1968 (2019).
12. Fan, L. et al. Strategies in catalysts and electrolyzer design for electrochemical $CO_2$ reduction toward $C_{2+}$ products. *Sci. Adv.* **6**, eaay3111 (2020).
13. Han, G. H. et al. Recent advances in electrochemical, photochemical, and photoelectrochemical reduction of $CO_2$ to $C_{2+}$ products. *Small* **19**, 2205765 (2023).
14. Sano, N. et al. Polyviologen hydrogel with high-rate capability for anodes toward an aqueous electrolyte-type and organic-based rechargeable device. *ACS Appl. Mater. Interfaces* **5**, 1355–1361 (2013).
15. Ding, J. et al. Viologen-inspired functional materials: synthetic strategies and applications. *J. Mater. Chem. A* **7**, 23337–23360 (2019).
16. Tachikawa, T., Tojo, S., Fujitsuka, M. & Majima, T. Direct observation of the one-electron reduction of methyl viologen mediated by the $CO_2$ radical anion during $TiO_2$ photocatalytic reactions. *Langmuir* **20**, 9441–9444 (2004).
17. Ranjan, R. et al. Reversible electrochemical trapping of carbon dioxide using 4,4′-bipyridine that does not require thermal activation. *J. Phys. Chem. Lett.* **6**, 4943–4946 (2015).
18. Li, Y. C. et al. $CO_2$ electroreduction from carbonate electrolyte. *ACS Energy Lett.* **4**, 1427–1431 (2019).
19. Lee, G. et al. $CO_2$ electroreduction to multicarbon products from carbonate capture liquid. *Joule* **7**, 1277–1288 (2023).
20. Hatakeyama-Sato, K. et al. Hydrophilic organic redox-active polymer nanoparticles for higher energy density flow batteries. *ACS Appl. Polym. Mater.* **1**, 188–196 (2019).
21. Tan, Y. C., Lee, K. B., Song, H. & Oh, J. Modulating local $CO_2$ concentration as a general strategy for enhancing C–C coupling in $CO_2$ electroreduction. *Joule* **4**, 1104–1120 (2020).
22. Wang, J. et al. Selective $CO_2$ electrochemical reduction enabled by a tricomponent copolymer modifier on a copper surface. *J. Am. Chem. Soc.* **143**, 2857–2865 (2021).
23. Xie, Y. et al. High carbon utilization in $CO_2$ reduction to multi-carbon products in acidic media. *Nat. Catal.* **5**, 564–570 (2022).
24. Li, W. et al. Bifunctional ionomers for efficient co-electrolysis of $CO_2$ and pure water towards ethylene production at industrial-scale current densities. *Nat. Energy* **7**, 835–843 (2022).
25. Li, X., Zhao, X., Liu, Y., Hatton, T. A. & Liu, Y. Redox-tunable Lewis bases for electrochemical carbon dioxide capture. *Nat. Energy* **7**, 1065–1075 (2022).
26. Wang, X. et al. Efficient electrosynthesis of n-propanol from carbon monoxide using a Ag-Ru-Cu catalyst. *Nat. Energy* **7**, 170–176 (2022).
27. Chernyshova, I. V., Somasundaran, P. & Ponnurangam, S. On the origin of the elusive first intermediate of $CO_2$ electroreduction. *E* **115**, 9261–E9270 (2018).
28. Lee, J.-E. et al. In situ FTIR study of $CO_2$ reduction on inorganic analogues of carbon monoxide dehydrogenase. *Chem. Commun.* **57**, 3267–3270 (2021).
29. Li, X., Wang, S., Li, L., Sun, Y. & Xie, Y. Progress and perspective for in situ studies of $CO_2$ reduction. *J. Am. Chem. Soc.* **142**, 9567–9581 (2020).
30. Huang, J. E. et al. $CO_2$ electrolysis to multicarbon products in strong acid. *Science* **372**, 1074–1078 (2021).
31. Zhao, Y. et al. Conversion of $CO_2$ to multicarbon products in strong acid by controlling the catalyst microenvironment. *Nat. Synth.* **2**, 403–412 (2023).
32. Doherty, C. M., Caruso, R. A., Smarsly, B. M. & Drummond, C. J. Colloidal crystal templating to produce hierarchically porous $LiFePO_4$ electrode materials for high power lithium ion batteries. *Chem. Mater.* **21**, 2895–2903 (2009).
33. Ryu, J., Ku, S. H., Lee, H. & Park, C. B. Mussel-inspired polydopamine coating as a universal route to hydroxyapatite crystallization. *Adv. Funct. Mater.* **20**, 2132–2139 (2010).
34. Hess, B., Kutzner, C., van der Spoel, D. & Lindahl, E. GROMACS 4: Algorithms for highly efficient, load-balanced, and scalable molecular simulation. *J. Chem. Theory Comput.* **4**, 435–447 (2008).
35. Wang, J., Wolf, R. M., Caldwell, J. W., Kollman, P. A. & Case, D. A. Development and testing of a general amber force field. *J. Comput. Chem.* **25**, 1157–1174 (2004).

36. Bayly, C. I., Cieplak, P., Cornell, W. & Kollman, P. A. A well-behaved electrostatic potential-based method using charge restraints for deriving atomic charges: the RESP model. *J. Phys. Chem.* **97**, 10269–10280 (1993).
37. Heinz, H., Vaia, R. A., Farmer, B. L. & Naik, R. R. Accurate simulation of surfaces and interfaces of face-centered cubic metals using 12–6 and 9–6 Lennard-Jones potentials. *J. Phys. Chem. C.* **112**, 17281–17290 (2008).
38. Bussi, G., Donadio, D. & Parrinello, M. Canonical sampling through velocity rescaling. *J. Chem. Phys.* **126**, 014101 (2007).
39. Parrinello, M. & Rahman, A. Crystal structure and pair potentials: A molecular-dynamics study. *Phys. Rev. Lett.* **45**, 1196–1199 (1980).
40. Hess, B., Bekker, H., Berendsen, H. J. C. & Fraaije, J. G. E. M. LINCS: A linear constraint solver for molecular simulations. *J. Comput. Chem.* **18**, 1463–1472 (1997).
41. Humphrey, W., Dalke, A. & Schulten, K. VMD: Visual molecular dynamics. *J. Mol. Graph.* **14**, 33–38 (1996).
42. Zhao, Y. & Truhlar, D. G. The M06 suite of density functionals for main group thermochemistry, thermochemical kinetics, noncovalent interactions, excited states, and transition elements: two new functionals and systematic testing of four M06-class functionals and 12 other functionals. *Theor. Chem. Acc.* **120**, 215–241 (2008).
43. Hay, P. J. & Wadt, W. R. Ab initio effective core potentials for molecular calculations. Potentials for K to Au including the outermost core orbitals. *J. Chem. Phys.* **82**, 299–310 (1985).
44. Mennucci, B., Cancès, E. & Tomasi, J. Evaluation of solvent effects in isotropic and anisotropic dielectrics and in ionic solutions with a unified integral equation method: Theoretical bases, computational implementation, and numerical applications. *J. Phys. Chem. B* **101**, 10506–10517 (1997).
45. Liu, W. et al. Electrochemical $CO_2$ reduction to ethylene by ultrathin CuO nanoplate arrays. *Nat. Commun.* **13**, 1877 (2022).

## Acknowledgements

This work was financially supported by the Ontario Research Foundation: Research Excellence Program, the Canada Research Chairs Program and the Natural Sciences and Engineering Research Council of Canada (NSERC).

## Author contributions

E.H.S. and D.S. supervised the work. J.Z. contributed to the main idea and designed experiments. Y.C. (Yufei Cao) and P.O. contributed to the DFT calculations. G.L. contributed to the electrochemical experiments and energy analysis. Y.Z conducted in-situ characterization experiments. S.L., E.S., R.D., K.X., C.T., Y.C. (Yuanjun Chen), X.L., Y.C.X., A.S.Z., R.K.M., S.P., C.P.O., J.G., X.Z. contributed to data analysis, discussions, and manuscript preparation.

## Competing interests

Authors declare that they have no competing interests.

## Additional information

**Supplementary information** The online version contains supplementary material available at https://doi.org/10.1038/s41467-025-58756-9.

**Correspondence** and requests for materials should be addressed to David Sinton or Edward H. Sargent.

**Peer review information** *Nature Communications* thanks Tao Cheng, and the other, anonymous, reviewers for their contribution to the peer review of this work. A peer review file is available.

**Reprints and permissions information** is available at http://www.nature.com/reprints

**Publisher's note** Springer Nature remains neutral with regard to jurisdictional claims in published maps and institutional affiliations.



[1]Department of Electrical and Computer Engineering, University of Toronto, 35 St George 7 Street, Toronto, Ontario M5S 1A4, Canada. [2]Department of Mechanical and Industrial Engineering, University of Toronto, 5 King's 11 College Road, Toronto, Ontario M5S 3G8, Canada. [3]School of Mathematical and Physical Sciences, Faculty of Science, University of Technology Sydney, Broadway, Sydney, NSW 2007, Australia. [4]Key Lab for Industrial Biocatalysis, Ministry of Education, Department of Chemical Engineering, Tsinghua University, Beijing 100084, China. [5]School of Chemical and Biological Engineering, Seoul National University, Seoul, Republic of Korea. [6]School of Chemistry and Chemical Engineering, South China University of Technology, Guangzhou 510640, China. [7]These authors contributed equally: Jinqiang Zhang, Yufei Cao, Pengfei Ou, Geonhui Lee, Yufei Zhao. ✉e-mail: sinton@mie.utoronto.ca; ted.sargent@utoronto.ca